EFFECTS OF AMMONIA ADDITION ON COMBUSTION CHARACTERISTICS IN PARTIALLY-PREMIXED SWIRLING AMMONIA/METHANE/AIR FLAME

by

Junqing ZHANG, Chunjie SUI*, Lianjie ZHANG, Jieyu JIANG, and Bin ZHANG

College of Electromechanical Engineering,
Qingdao University of Science and Technology, Qingdao, China

Original scientific paper
https://doi.org/10.2298/TSCI211020013Z

Ammonia combustion has received intense research interest recently for its potential to reduce CO_2 emission. This study aims to investigate the turbulent combustion characteristics in a bluff-body burner for CH_4/NH_3 mixtures with different ammonia blending ratios (15%, 30%, and 45% by mole fraction) through large eddy simulation and experiments. The simulations are conducted using openFOAM with a low Mach number solver and the partially stirred reactor combustion model with a detailed reaction mechanism. The flow field of one typical case is measured using the particle image velocimetry technique to verify the accuracy of the numerical results. The combustion characteristics are discussed. As the ammonia blending ratio increases, the flame height shortens, the flame color gradually changes from blue to orange, and the intermittent local quenching zone moves upstream, indicating that the combustion is becoming unstable. Meanwhile, the flow fields exhibit similar characteristics though the ammonia concentration varies greatly. The CO and NO emissions are also discussed. The CO emission decreases and the NO emission increases as the ammonia blending ratio increases.

Key words*: large eddy simulation, ammonia addition, swirling flame, particle image velocimetry, combustion characteristics*

Introduction

Despite the current research interest on the supply of energy from different low cost resources with low CO_2 emissions, the major global energy supply still depends on fossil fuels. The pollutant emissions from the combustion of fossil fuels have damaged the environment, and the massive CO_2 emissions have been regarded as an important contributor to global climate change [1].

Many researchers have been working on the development of clean and carbon-free fuels in recent decades, and H_2 has been regarded as one of the key fuels. However, the economical storage and transportation of H_2 is still a big challenge to its use because H_2 has active molecules, an explosive nature, and a high storage pressure and needs specially processed storage containers [2].

Ammonia (NH_3) combustion has received intense research interest recently because of its potential to reduce CO_2 emission [3]. The NH_3 can be produced from renewable energy

* Corresponding author, e-mail: suichunjie123@163.com

sources [4], and the technologies related to its production, transportation, and storage have been established well. In addition, NH_3 can be easily liquefied and stored compared with H_2 [5].

Attempts have been made to use ammonia as a fuel since the 1940's, and NH_3 was added to coal gas to drive the reciprocating engine during the World War II. However, NH_3 combustion applications have been discouraged recently mainly because of the low flammability of NH_3/air mixtures and the high fuel NO_x emission in the flames [2]. The low flammability of NH_3 combustion is reflected in the high minimum ignition energy, the narrow equivalence ratio limit, and the low laminar burning velocity [6], which may also lead to combustion instability. To address the low flammability of NH_3 combustion, considerable research on NH_3-containing fuel mixtures, such as the NH_3/CH_4 and NH_3/H_2 mixtures, has been conducted.

Kumar and Meyer [7] performed a combined experimental and modelling study on premixed H_2/NH_3/air jet flames and found that OH is the key radical of NH_3 decomposition. Um *et al.* [8] conducted experimental and numerical research on non-premixed H_2/NH_3/air jet flames and concluded that the flame stability limits decrease significantly and the flame length increases as the NH_3 blending ratio increases.

Okafor *et al.* [9, 10] experimentally and numerically studied CH_4/NH_3/air premixed flames, and their results show that the laminar burning velocity decreases, the NO_x emission increases, and the flames gradually change from blue to orange with the increase in NH_3 blending ratio. Okafor *et al.* [11] also numerically investigated CH_4/NH_3/air premixed swirling flames in a micro gas turbine. They found that two-stage rich-lean combustion controls the NO_x emissions fueled with CH_4/NH_3 mixtures. Zhang *et al.* [12] investigated the blow-off and the flame macro-structure transition behavior of both NH_3/air flame and NH_3/CH_4/air flame in a swirl-stabilized combustor. Their results show that the NH_3 flame possesses a poor lean flame stability limit, which can be largely extended by adding CH_4 in the fuel.

Although some investigations into swirling CH_4/NH_3 combustion have been conducted, most studies based on experiments. The studies using large eddy simulation (LES) on the combustion characteristics are limited, requiring further study as the theoretical foundation of combustion application. Therefore, this study aims to perform LES and experiments to investigate the effects of the NH_3 blending ratio on the combustion characteristics (including flame structure, combustion stability and emissions) in partially-premixed swirling CH_4/NH_3/air combustion, and find the proper working condition with low emission and stable combustion. The flow field of a typical case is measured using the particle image velocimetry (PIV) technique to verify the accuracy of the numerical results.

Numerical methodology

Large eddy simulation

In the present work, LES is performed using the open source CFD toolbox, OpenFOAM (version 7). Considering that the Mach number is far less than 0.3, a modified incompressible solver based on reactingFoam is used. The gas mixture is presumed to be ideal and linearly viscous, with Fourier heat conduction and Fickian diffusion. The laminar viscosity is modelled by Sutherland's law. The governing equations are the filtered mass, momentum, species, and enthalpy equations [13]. In the LES method, the large-scale eddies are resolved directly, while the small-scale eddies are modeled with the turbulence model. The sub-grid stress tensor is modeled by the dynamic Smagorinsky model [14].

The partially stirred reactor (PaSR) model is used to solve the interaction between the turbulence and the chemical reaction in LES. This model regards each computing grid as a small reactor, where fuel and oxygen are mixed and chemical reactions occur. In the PaSR

model, each LES cell can be divided into fine structures, where mixing and reactions are assumed to take place, and the surroundings, dominated by large-scale coherent flow structures. The relative sizes of the two parts in the cell are governed by reactive volume fraction, $\kappa = \tau_c/(\tau_c + \tau_m)$. Here, τ_m is the turbulent time scale and τ_c is the chemical time scale determineby the reaction rate. In this study, τ_m is modelled with a modified model based on sub-grid velocity stretch time scale τ_Δ and Kolmogorov time scale τ_κ [15, 16]. The modified PaSR model has been successfully applied in turbulent combustion under a high Reynolds number [15, 16].

Reaction mechanism

Extensive research has explored ammonia combustion, especially in NH_4-containing mixture chemical mechanisms. The comparison of NH_4-containing fuel chemical mechanisms is presented in tab. 1. Kobayashi *et al*. [2] validated different reaction mechanisms through 1-D simulation and found that the Okafor2018 mechanism satisfactorily models the burning velocity of CH_4/NH_3/air flames, and provides proper predictions of the extinction stretch rate and the NO concentration. In this study, the Okafor2019 mechanism (with 42 species and 130 reactions) was adopted after measuring the computing resources cost and the prediction accuracy. The Okafor2019 mechanism was optimized from the Okafor2018 mechanism, developed with measured values of the unstretched laminar burning velocity of and species concentration in CH_4/NH_3/air and NH_3/air flames [10]. The Okafor2019 mechanism has been successfully used to predict the flame structure and NO emissions in a micro gas-turbine-fueled CH_4/NH_3 mixture by LES [11].

Table 1. Comparison of ammonia-containing fuel chemical mechanisms

Mechanism	Species/reactions	Fuel
[17]	19/73	NH_3
[18]	55/278	NH_3/H_2
[19]	41/250	NH_3/CO
[20]	129/1231	$NH_3/CH_4/H_2$
[21]	84/703	NH_3/CH_4
[9]	59/356	NH_3/CH_4
[10]	42/130	NH_3/CH_4
[22]	53/325	CH_4 (including NH_3 related reactions)

Flow configuration

Experimental device

To study the partially-premixed swirling CH_4/NH_3/air flame in a bluff-body burner with different NH_4 blending ratios, this study performed experiments for simulation validation. As shown in fig. 1, the diameter of the fuel inlet on the nozzle, D, is 2 mm, and the 10-vane swirler with a vane angle of 45° is installed on the outside of the nozzle, with an inner diameter of 16 mm and an outer diameter of 36 mm (S = 0.76). Swirl number, S, is defined as $S = 2/3(1 - Z^3)\tan\alpha/(1 - Z^2)$, in which, Z is the ratio of inner diameter to outer diameter, and α is the vane angle.

The schematic of the experimental set-up is shown in fig. 2. The experimental set-up is composed of the combustion and optical measurement systems. The combustion system includes the fuel supply, the air supply, and the burner. The NH_4, CH_4, and premixed air-flow out

from these gas bottles and, respectively pass through a pressure reducing valve, a ball valve, and a mass-flow controller into the fuel tube. The swirling air is compressed by the compressor and stored in the air bottle. To conveniently adjust the concentration of tracer particles, the compressed air is divided into two channels after flowing through a pressure reducing valve, a ball valve, and a mass-flow controller. One channel passes through a needle valve, leading to the particle mixer. Then, the air and the tracer particles enter the mixing chamber of the burner and mix thoroughly. The measurement errors of the mass-flow controllers are below 1%. The optical measurement system includes a double pulse Nd:YAG laser, a PIV-CCD camera, a synchronizer, and a computer and is implemented according to the PIV measurement technology [23]. More information about the optical measurement system can be found in reference [24].

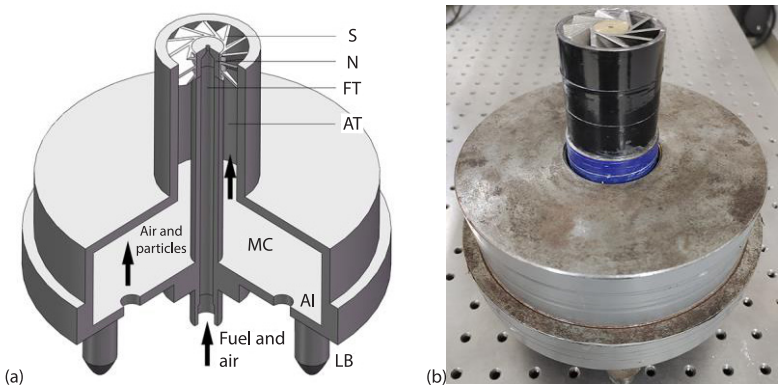

Figure 1. (a) Structural diagram of the burner: *S – swirler, AT – air tube, AI – air inlet, FT – fuel tube, N – nozzle, LB – leveling bolts, MC – mixing chamber* **and (b) the burner used in the experiment**

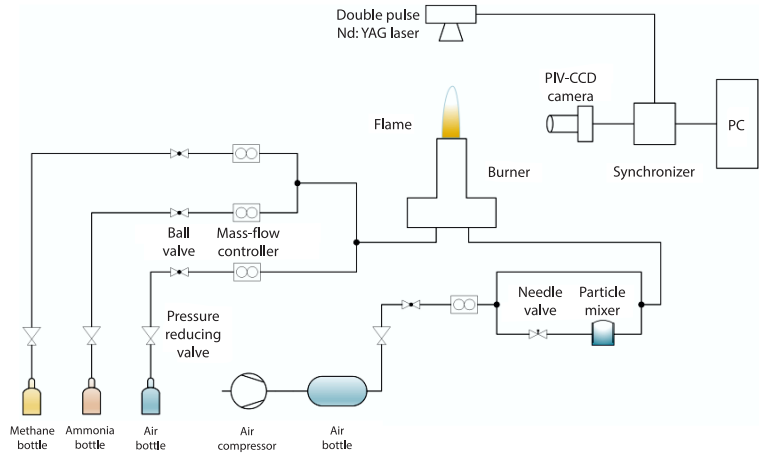

Figure 2. Schematic of the experimental set-up

The studied cases with a range of NH_3 blending ratios (15%, 30%, and 45% by mole fraction) are summarized in tab. 2. Here, Φ_{in} refers to the equivalence ratio of the fuel stream, while $\Phi_{overall}$ refers to the equivalence ratio obtained based on the total air and fuel supplied to the combustion area. The oxidizer stream has the same values for all cases: $T_{air\text{-}swirling}$ = 300 K, $Q_{air\text{-}swirling}$ = 60 slm, and environmental condition also has the same values: T_e = 300 K,

p_e = 101325 Pa. In the experiment, the combustion proceeded stably without blow out, and the experimental results are presented in detail in section *Experimental validation* to verify the accuracy of the numerical results.

Table 2. Inflow conditions of the fuel stream for different cases

Case	T_{fuel}	X_{NH_3}	Q_{NH_3}	Q_{CH_4}	$Q_{air\text{-}premixed}$	Φ_{in}	$\Phi_{overall}$
A	300 K	0.15	45 sccm	255 sccm	300 sccm	8.63	0.0429
B	300 K	0.3	90 sccm	210 sccm	300 sccm	7.73	0.0385
C	300 K	0.45	135 sccm	165 sccm	300 sccm	6.84	0.0340

Computational details

Figure 3 shows the schematics of the computational domain. The computational domain for the LES encompasses a short section of an inflow passage and an open cylindrical combustion area with a diameter of 108 mm and a length of 108 mm. The black line indicates a *wall* boundary, and the blue line indicates a *patch* boundary. The boundary conditions in the LES are listed in tab. 3. Axial inlet velocities u_{fuel} = 3.55 m/s and u_{air} = 1.35 m/s (with tangential inlet velocity w_{air} = 1.35 m/s) are provided according to the mass-flow rates in tab. 2. The computational domain adopted a hexahedral mesh with optimization in the area where reactions occur. To check the grid independence, we performed simulations for cold flow with three mesh schemes. According to fig. 4(a), the coarse mesh (with 0.25 million cells) yielded obviously different results from the others, whereas the results from the mid mesh (with 0.5 million cells) were almost the same as those from the fine mesh (with 1 million cells). Thus, the mesh with 0.5 million grids with an average grid spacing of 0.5 mm was used, as shown in fig. 4(b).

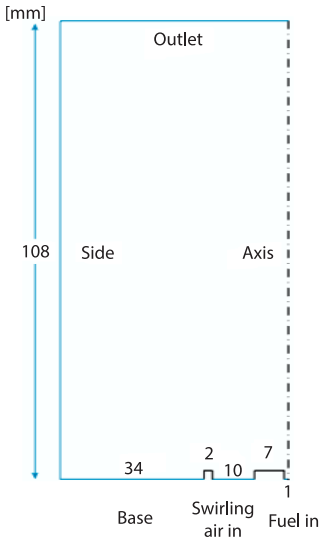

Figure 3. Computational domain

Table 3. Boundary conditions in simulation

	Pressure	Velocity	Temperature
Wall	zeroGradient	noSlip	zeroGradient
Fuel-in	zeroGradient	fixedValue	fixedValue
Swirling air-in	zeroGradient	fixedValue	fixedValue
Base	zeroGradient	fixedValue	zeroGradient
Side	totalPressure	pressureInletOutletVelocity	inletOutlet
Outlet	zeroGradient	inletOutlet	inletOutlet

The simulations of the three cases listed in tab. 2 were conducted using OpenFOAM, with an unstructured collocated finite volume method. The solver employs the second-order semi-implicit Crank-Nicolson scheme coupled with a fraction of the first-order implicit Euler scheme as the time discretized method. The algorithm for pressure-velocity coupling is based on the PIMPLE method (combining the SIMPLE method [25], and the PISO method [26]),

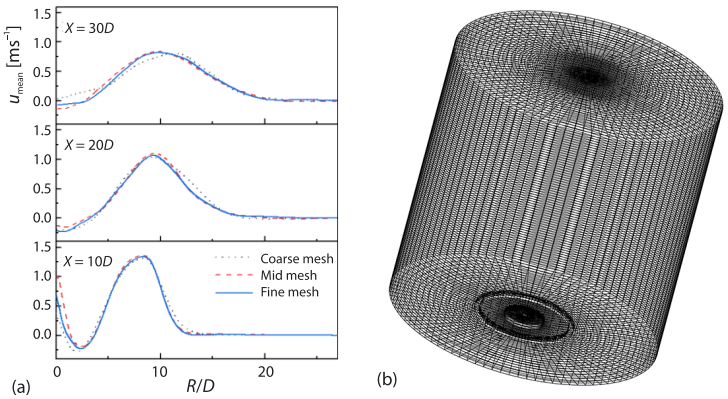

Figure 4. Comparison of radial profiles of mean velocity obtained by three mesh schemes (a) and schematics of mesh (b)

which is suitable for transient simulations. The convection divergence terms are discretized using a second-order central difference scheme with the Sweby flux limiter. Given the large amount of computation involved in the LES, a parallel strategy was adopted herein.

The simulation of each case ran until the flow time reached 1.5 seconds to obtain full development. The residuals for species and enthalpy should be less than 10^{-6} while other equations are below 10^{-3}. Then, the statistical data were obtained from 1.5-2.0 seconds. All the cases used an adjustable time step (limited by the max Courant number 0.5 and the max time step 10^{-5} second) to guarantee computational stability and capture the dynamic processes of combustion. The simulations were completed on an intel parallel cluster, with one case consuming approximately 5000 CPU hours to obtain the final results.

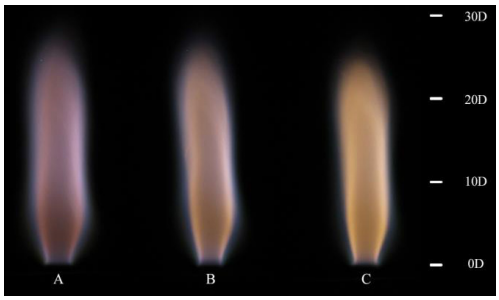

Figure 5. Experimental flame images, 0.5 second exposure time

Experimental validation

The experimental flame images captured by a digital camera (Nikon D5600) are shown in fig. 5. The flame height slightly shortened and the flame color gradually changed from blue to orange as X_{NH_3} increased. The blue region is associated with CH and CO_2 chemiluminescence [27], and the orange chemiluminescence was due to the NH_2-α band and super-heated H_2O vapor spectra [6].

In the experiment, the flow field of Case A was measured using the PIV technique to verify the accuracy of the LES. Figure 6 shows the instantaneous distributions of tracer particles and the experimental flow field of Case A. The main flow structures are successfully captured by PIV technique, including shear layers and the central re-circulation zone (CRZ) near the nozzle. The CRZ enhances the mixing process of fuel and air and provides hot flue gas with low velocity to the flame root, which provides a dominant stabilization mechanism of the swirling flame [28, 29]. It could be deduced that with lower swirl number, it cannot provide enough hot flue gas to the flame root to stabilize the combustion process, while the higher swirl number might be detrimental to the stability of the flame using ammonia [30].

Figure 7 shows the axial and the radial profiles of the mean velocity of Case A obtained by the experiment and the LES. The figure indicates that the LES successfully captured the double-peak flow structure, and the difference between the experiment and the LES is mi-

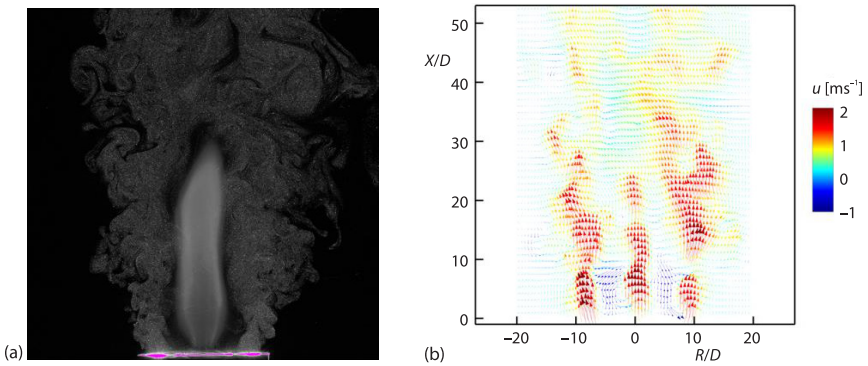

Figure 6. Instantaneous distributions of (a) tracer particles and (b) experimental flow field

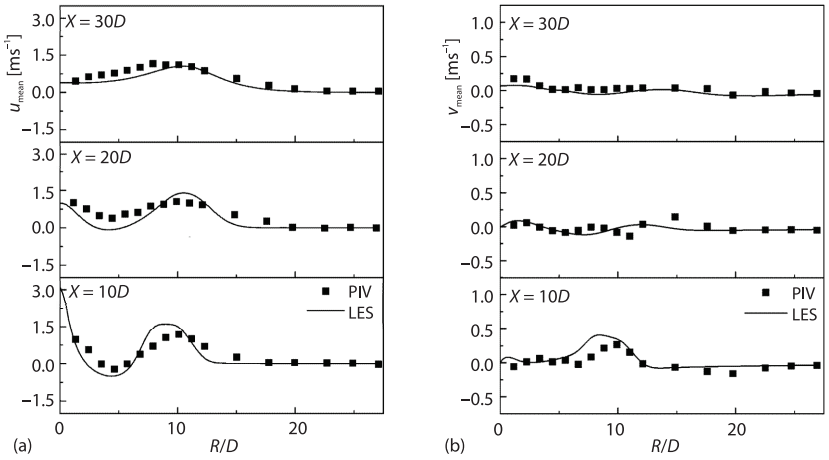

Figure 7. Comparison of radial profiles of mean velocity obtained by PIV experiment and LES

nor. The experimental results show a good prediction capability on the chemical mechanism and flow dynamics of the current simulation.

Results and discussion

Flame structure

Figure 8 shows the computed instantaneous 2-D distributions of H_2 and OH. Figure 8(a) indicates that the global high H_2 concentration zone distributes near downstream of the flame in each case. The H_2 concentration decreased slightly as X_{NH_3} increased, though a decrease in H_2 production from the CH_4 chemistry tends to be compensated by an increase in production from the NH_3 chemistry. As shown in fig. 8(b), the global high OH concentration zone distributes near the oxygen side of the flame surface (determined by heat release rate in the simulation, which will be detailed in section *Turbulence-chemistry interaction*) in each case. According to the previous research performed by Okafor *et al.* [11], the H_2 and CO consumption leads to the production of OH. The OH concentration also decreased with the X_{NH_3} increasing because the H_2 and CO emissions decreased.

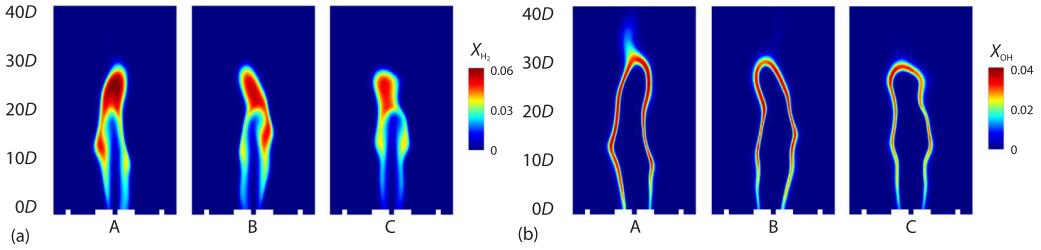

Figure 8. Computed instantaneous 2-D distributions of H_2 and OH

The variations of time-averaged H_2 and OH with the progress variable at different axial positions are shown in fig. 9. In the present research, the progress variable, c, is defined as $c = (T - T_e)/(T_{ad} - T_e)$. Here, T is the local temperature, obtained from simulation, T_e is the environmental temperature, $T_e = 300$ K, and T_{ad} is the adiabatic flame temperature, as listed in tab. 4.

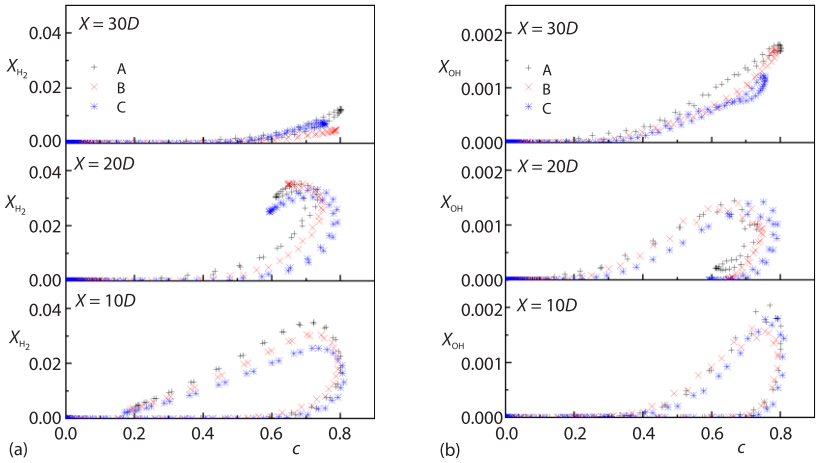

Figure 9. Variations of time-averaged H_2 and OH with progress variable at different positions

For $X = 10D$, when $c < 0.75$, H_2 was produced as an intermediate product mainly through the reactions of NH_3 with H and CH_4 with H. Thus, the H_2 concentration increased with the progress variable. When $0.75 < c < 0.8$, H_2 was consumed quickly with OH. Thus, the H_2 concentration decreased sharply with the increasing progress variable. The three cases have similar trends of H_2 distribution. However, the maximum H_2 concentration and the growth rate of H_2 decreased as X_{NH3} increased, indicating the low flammability of NH_3 combustion. The three cases also have similar trends of OH distribution. When $c < 0.75$, OH was produced as an intermediate radical mainly through the following reaction: $H + O_2 = OH + O$. This reaction is highly sensitive to temperature [31], thereby increasing the OH concentration quickly with the progress variable. When $0.75 < c < 0.8$, OH was consumed quickly with H_2 and CO. Thus, the OH concentration decreased sharply with the increasing progress variable.

For $X = 20D$, H_2 was produced as an intermediate product mainly through the reactions of NH_2 with H and CH_2O with H. The high H_2 concentration zone distributes near $c = 0.65$, and the low OH concentration zone also distributes in the same region. Thus, H_2 was not consumed quickly with OH here. When $c < 0.7$, OH increased with the progress variable. When $0.7 < c < 0.8$, OH decreased sharply with the increasing progress variable.

Table 4. Laminar flame characteristics for different ammonia/methane blending ratio

X_{NH_3}	T_{ad}	S_u	δ_u	τ_c
0.15	2204 K	0.304 m/s	0.533 mm	1.75 ms
0.3	2185 K	0.255 m/s	0.621mm	2.44 ms
0.45	2168 K	0.210 m/s	0.734 mm	3.50 ms

For $X = 30D$, the H_2 concentration increased slightly with the progress variable, and the maximum H_2 concentration dropped here because NH_2 and CH_2O were nearly consumed in the three cases. The OH concentration increased with the progress variable, and the maximum OH concentration increased greatly because the H_2 and CO concentrations dropped here. The maximum OH concentration in Case C is lower than those in the other cases because Case C has a shorter flame length, and the high OH concentration zone distributes near the flame surface.

Turbulence-chemistry interaction

The Karlovitz number is an important dimensionless number reflecting turbulence–chemistry interaction, defined as $\mathrm{Ka} = \tau_c/\tau_\kappa \approx (\delta_u/S_u)(\nu/(\varepsilon_t)^{0.5}$. The laminar flame speed, S_u, and the laminar flame thickness, δ_u, were computed by ANSYS Chemkin-Pro with the Okafor2019 mechanism for different ammonia/methane blending ratio, tab. 4.

Figure 10 shows the computed instantaneous 2-D distributions of heat release rate and indicates the Karlovitz number. As shown in fig. 10, Cases A and B have similar trends of heat release rate distribution, and the heat release rate decreased near the leading edge of the flame surface because the strain rate increased sharply near the leading edge of the flame surface, and intermittent local quenching occurs here. However, Case C exhibited an obviously different trend from the other cases. In Case C, intermittent local quenching occurred near the right side of the downstream flame surface instead of the leading edge of the flame surface. This phenomenon is mainly caused by the turbulence–chemistry interaction, that is, the turbulent vortex structure could easily penetrate the flame surface and affect the internal flame structure with the increasing Karlovitz number. With X_{NH_3} increasing, that is, increasing Karlovitz number, the strain rate of the flame was obviously affected by the turbulent vortex structure. Consequently, the intermittent local quenching zone moved upstream and the combustion became unstable. Furthermore, the reactions will be promoted at weak reaction regions and suppressed at intense reaction regions with the increasing Karlovitz number [32]. Hence, the high heat release rate zone shrunk at the left side of the flame surface in Case C.

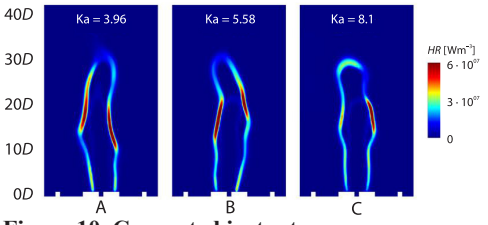

Figure 10. Computed instantaneous 2-D distributions of heat release rate (Ka are indicated)

The radial profiles of the mean and fluctuating axial velocity obtained by the LES are shown in fig. 11. Figure 11(a) indicates that the mean axial velocity distribution presents the same trend though the ammonia concentration varied greatly. For $X = 10D$, the axial velocity was mainly affected by the shear layers, the inlet velocity, and the CRZ. The positions of the shear layers could be accurately captured, including the inner shear layer ($0.5D < R < 2D$), the outer shear layer ($6D < R < 8D$), and the surrounding shear layer ($10D < R < 13D$). The CRZ ($2D < R < 6D$) was also observed due to the negative axial velocity in this region, and the highest velocity at the central line was dominated by the inlet velocity. For $X = 20D$, the axial

velocity was determined by the competition between the swirling motion and the combustion heat release. The swirling motion diverges the flow and reduces the axial velocity, while the combustion heat release expands the gas volume and increases the axial flow velocity. The influence of the shear layers and the inlet velocity on axial velocity decreased, and the CRZ also disappeared here. For $X = 30D$, the axial velocity was mainly affected by the swirling motion because the combustion heat release quickly decreased here. Furthermore, the inner shear layer and the outer shear layer also disappeared because the axial velocity of the mainstream decreased.

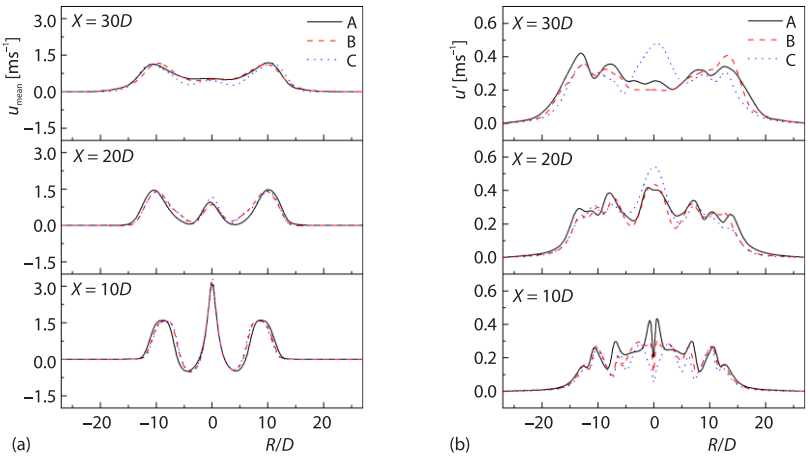

Figure 11. Radial profiles of mean and fluctuating axial velocity obtained by LES, (a) u_{mean} and (b) u'

As shown in fig. 11(b), the fluctuating axial velocity displayed an obviously different distribution trend, which is related to heat release fluctuations and the combustion instability. For $X = 10D$, the peaks of the fluctuating axial velocity are related to the shear layers, and the locations of the shear layers are consistent with fig. 11(a). In addition, the fluctuating axial velocity near the central line obviously decreased from Case A to Case C. For $X = 20D$ and $X = 30D$, the high Karlovitz number of Case C led to intense chemistry–turbulence interaction, and the reactions were promoted at the weak reaction regions and suppressed at the intense reaction regions, as shown in fig. 8. Hence, the heat release fluctuations in Case C became higher than those in the other cases, resulting in a high fluctuating axial velocity downstream the reaction zone.

The CO and NO emissions

The CO emission has a harmful effect on human health, and high fuel NO emission is one of the major challenges in NH_3 combustion. Thus, CO and NO emissions are evaluated in this section. The variations of CO and NO with the progress variable are shown in fig. 12.

In the Okafor2019 mechanism, CO is produced as an intermediate product mainly from HCO and CH_3 consumption and consumed with OH and the NO emission was mainly determined by NH_i and OH. The O/OH radical promotes HNO production through the $NH_2 + O = HNO + H$ and $NH + OH = HNO + H$ reactions, and HNO contributes approximately 70% to the NO production via the $HNO + H = NO + H_2$ reaction [10]. When X_{NH_3} was below 30%, the NO formation was insensitive to the OH concentration, and was sensitive to the NH_i concentration, because the NO production was limited by the low NH_i concentration. Similarly,

the CO formation was also insensitive to the CH_3, and was sensitive to the OH, because of high CH_3 concentration. When X_{NH3} reached 45%, the NO formation became sensitive to OH though OH concentration decreased (as shown in fig. 9), and the CO formation became sensitive to CH_3. Hence, CO concentration quickly decreased and NO concentration increased.

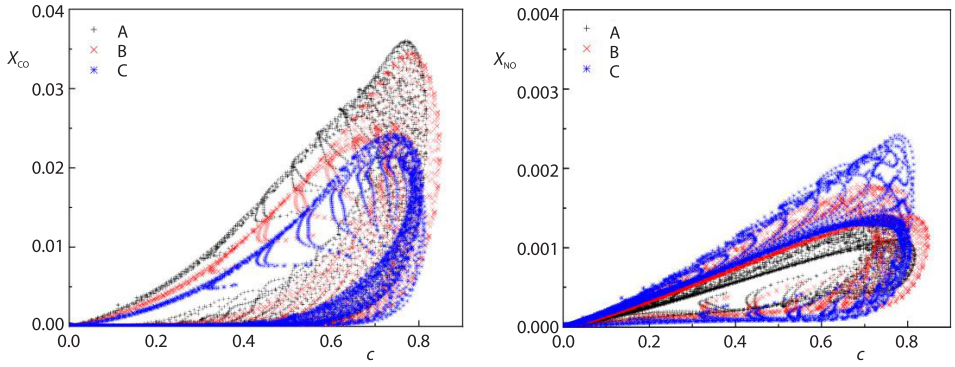

Figure 12. Variations of CO and NO with progress variable

Figure 13 shows the instantaneous distributions of CO and NO, and the space-time-averaged CO and NO species concentration at 16% O_2 concentration of the exit are indicated. The distribution of CO is similar to that of H_2 because CO and H_2 were consumed with OH via the $H_2 + OH = H + H_2O$ and $CO + OH = H + CO_2$ reactions.

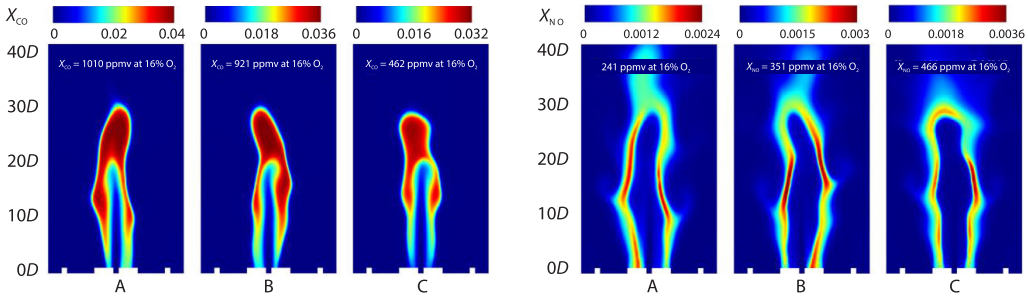

Figure 13. Instantaneous distributions of CO and NO (space-time-averaged CO and NO species concentration at 16% O_2 concentration of the exit are indicated)

The high NO concentration zone is related to the high heat release rate zone because the NO formation in NH_3/CH_4 combustion was highly sensitive to temperature, which is consistent with the result in fig. 12 (NO was mainly distributed at $c > 0.7$). This phenomenon was also observed in the previous research performed by Somarathne *et al.* [31].

Conclusions

In this work, the effects of NH_3 addition in partially-premixed swirling NH_3/CH_4/air combustion in a bluff-body burner were investigated by LES and experiments. The main conclusions are as follows.

- The flame height slightly decreased and the flame color gradually changed from blue to orange as the ammonia blending ratio increased.
- The flow structures obtained by the LES are consistent with those of the experiment. Furthermore, the concentrations of H_2 and OH decreased as the NH_3 blending ratio increased.

- When X_{NH3} was below 30%, intermittent local quenching occurred near the leading edge of the flame surface. When X_{NH3} reached 45%, the intermittent local quenching zone moved upstream and the combustion became unstable due to the increasing Karlovitz number.
- The CO emission decreases and the NO emission increases as the NH_3 blending ratio increases. But CO emission was insensitive to the CH_3 when X_{NH3} was below 30%.

In conclusion, the lower NH_3 blending ratio cannot effectively suppress CO emission, while the higher NH_3 blending ratio will lead to combustion instability and higher NO emission. Therefore, the proper NH_3 blending ratio needs to be assessed to control emissions and ensure combustion stability. These results would be useful in gas turbine for choosing proper NH_3 blending ratio in NH_3/CH_4/air combustion.

Acknowledgment

This research was supported by the Natural Science Foundation of Shandong Province of China (No. ZR2021ME131).

Nomenclature

c – progress variable, [–]
D – diameter of the fuel inlet, [mm]
p – pressure, [Pa]
Q_k – mass-flow rate of species k, [sccm]
R – radial axis
S – swirl number, [–]
S_u – laminar flame speed, [$m^{-1}s^{-1}$]
T – temperature, [K]
u, v w – axial, radial, tangential velocity, [$m^{-1}s^{-1}$]
X_k – mole fraction of species k, [–]

Greek symbols

α – Vane angle, [–]
δ_u – laminar flame thickness, [mm]
ε_i – sub-grid dissipation rate, [m^2s^{-3}]
ν – laminar kinematic viscosity, [Pa·s]
τ_c – chemical time scale, [ms]
τ_κ – Kolmogorov time scale, [ms]
τ_m – turbulent time scale, [ms]
τ_Δ – sub-grid velocity stretch time scale, [ms]
Φ – equivalence ratio, [–]

References

[1] Jiang, J., *et al*., A Computational Study of Preferential Diffusion and Scalar Transport in Non-Premixed Hydrogen-Air Flames, *Int. J. Hydrogen Energy*, *40* (2015), 45, pp. 15709-15722
[2] Kobayashi, H., *et al.*, Science and Technology of Ammonia Combustion, *Proc. Combust. Inst*., *37* (2019), 1, pp. 109-133
[3] Slefarski, R., et al., Experimental Study on Combustion of CH4/NH_3 Fuel Blends in an Industrial Furnace Operated in Flameless Conditions, *Thermal Science*, *24* (2020), 6A, pp. 3625-36235
[4] Michalsky, R., *et al*., Solar Thermochemical Production of Ammonia From Water, Air and Sunlight: Thermodynamic and Economic Analyses, *Energy*, *42* (2012), 1, pp. 251-260
[5] Yang, S. J., *et al*., Recent Advances in Hydrogen Storage Technologies Based on Nanoporous Carbon Materials, *Prog. Nat. Sci. Mater. Int*., *22* (2012), 6, pp. 631-638
[6] Hayakawa, A., *et al*., Laminar Burning Velocity and Markstein Length of Ammonia/Air Premixed Flames At Various Pressures, *Fuel*, *159* (2015), Nov., pp. 98-106
[7] Kumar, P., Meyer, T. R., Experimental and Modelling Study of Chemical-Kinetics Mechanisms For H_2-NH_3-Air Mixtures in Laminar Premixed Jet Flames, *Fuel*, *108* (2013), June, pp. 166-176
[8] Um, D. H., *et al.*, Combustion Stability Limits and NO_x Emissions of Non-Premixed Ammonia-Substituted Hydrogen-Air Flames, *Int. J. Hydrogen Energy*, *38* (2013), 34, pp. 14854-14865
[9] Okafor, E. C., *et al*., Experimental and Numerical Study of The Laminar Burning Velocity of CH_4-NH_3--Air Premixed Flames, *Combust. Flame*, *187* (2018), Jan., pp. 185-198
[10] Okafor, E. C., *et al*., Measurement and Modelling of the Laminar Burning Velocity of Methane-Ammonia-Air Flames at High Pressures Using a Reduced Reaction Mechanism, *Combust. Flame*, *204* (2019), June, pp. 162-175
[11] Okafor, E. C., *et al.*, Control of NO_x and Other Emissions in Micro Gas Turbine Combustors Fuelled with Mixtures of Methane and Ammonia, *Combust. Flame*, *211* (2020), Jan., pp. 406-416
[12] Zhang, M., *et al*., The Blow-off and Transient Characteristics of co-Firing Ammonia/Methane Fuels in a Swirl Combustor, *Proceedings of the Combustion Institute*, *38* (2021), 4, pp. 5859-5868

[13] Poinsot, T., Veynante, D., *Theoretical and Numerical Combustion*, 3rd ed., Edwards, Inc., Philadelphia, Penn., USA, 2012
[14] Germano, M., *et al*., A Dynamic Subgrid-Scale Eddy Viscosity Model, *Phys. Fluids A*, *3* (1991), 7, pp. 1760-1765
[15] Fureby, C., *et al*., A Computational Study of Supersonic Combustion in Strut Injector and Hypermixer Flow Fields, *Proc. Combust. Inst.*, *35* (2015), 2, pp. 2127-2135
[16] Sabelnikov, V., Fureby, C., The LES Combustion Modelling for High Re Flames Using A Multi-Phase Analogy, *Combust. Flame*, *160* (2013), 1, pp. 83-96
[17] Miller, J. A., *et al*., Kinetic Modelling of The Oxidation of Ammonia in Flames, *Combust. Sci. Technol*., *34* (1983), 1-6, pp. 149-176
[18] Mathieu, O., Petersen, E. L., Experimental and Modelling Study on the High-Temperature Oxidation of Ammonia and Related NO_x Chemistry, *Combust. Flame*, *162* (2015), 3, pp. 554-570
[19] Dagaut, P., *et al*., The Oxidation of Hydrogen Cyanide and Related Chemistry, *Prog. Energy Combust. Sci*., *34* (2008), 1, pp. 1-46
[20] Konnov, A. A., Implementation of the NCN Pathway of Prompt-NO Formation in the Detailed Reaction Mechanism, *Combust. Flame*, *156* (2009), 11, pp. 2093-2105
[21] Tian, Z., *et al*., An Experimental and Kinetic Modelling Study of Premixed $NH_3/CH_4/O_2$/Ar Flames at Low Pressure, *Combust. Flame*, *156* (2009), 7, pp. 1413-1426
[22] Smith, G. P., *et al*., The GRI-Mech 3.0, http://combustion.berkeley.edu/gri-mech/version30/text30.html
[23] Mergheni, M. A., *et al*., Swirl Effects on Dynamics Characteristics of a Coaxial Jet, *Thermal Science*, *21* (2017), 6, pp. 2543-2552
[24] Zhang, B., *et al*., Simultaneous Deflectionmography and PIV Measurements of Non-Premixed Combustion, *Opt. Lasers Eng*., *127* (2020), 105944
[25] Patankar, S. V., Spalding, D. B., A Calculation Procedure for Heat, Mass and Momentum Transfer in 3-D Parabolic Flows, *Int. J. Heat Mass Transf*., *15* (1972), 10, pp. 1787-1806
[26] Issa, R. I., *et al*., The Computation of Compressible and Incompressible Recirculating Flows by a Non-Iterative Implicit Scheme, *Journal Comput. Phys*., *62* (1986), 1, pp. 66-82
[27] Mikofski, M. A., *et al.*, Flame Height Measurement of Laminar Inverse Diffusion Flames, *Combust. Flame*, *146* (2006), 1-2, pp. 63-72
[28] Huang, Y., Yang, V., Dynamics and Stability of Lean-Premixed Swirl-Stabilized Combustion, *Prog. Energy Combust. Sci*., *35* (2009), 4, pp. 293-364
[29] Hung, H. Y., *et al*., Observation on a Fire Whirl in A Vertical Shaft Using High-Speed Camera and Associated Correlation Derived, *Thermal Science*, *25* (2021), 2A, pp. 1001-1012
[30] Valera-Medina, A., *et al*., Ammonia-Methane Combustion in Tangential Swirl Burners for Gas Turbine Power Generation, *Appl. Energy*, *185* (2017), 2, pp. 1362-1371
[31] Somarathne, K. D. K. A., *et al*., Effects of OH Concentration and Temperature on NO Emission Characteristics of Turbulent Non-Premixed CH_4/NH_3/Air Flames in a Two-Stage Gas Turbine Like Combustor at High Pressure, *Proc. Combust. Inst*., *38* (2021), 4, pp. 5163-5170
[32] Wang, X., *et al.*, Effects of Pressure and Karlovitz number on the Turbulence-Flame Interactions in Lean Premixed H_2/Air Flames, *Fuel*, *234* (2018), Dec., pp. 1293-1300

Paper submitted: October 20, 2021
Paper revised: December 30, 2021
Paper accepted: January 8, 2022